Lawrence Berkeley National Laboratory

Title
R&D Requirements, RF Gun Mode Studies, FEL-2 Steady-State Studies, Preliminary FEL-1
Time-Dependent Studies, and Preliminary Layout Option Investigation

Permalink
https://escholarship.org/uc/item/8rk8m5r8

Authors
Byrd, John
Corlett, John
Doolittle, Larry
et al.

Publication Date
2005-10-01

Third Deliverable to

The FERMI @ Elettra
Technical Optimization Study

entitled:

"R&D Requirements, RF Gun Mode Studies, FEL-2 Steady-State Studies, Preliminary FEL-1 Time-Dependent Studies, and Preliminary Layout Option Investigation"

submitted by:

Lawrence Berkeley National Laboratory
1 Cyclotron Road
Berkeley, CA 94720

John Byrd
John Corlett
Larry Doolittle
William Fawley
Steven Lidia
Gregory Penn
Alex Ratti
John Staples
Russell Wilcox
Jonathan Wurtele
Alexander Zholents

October 1, 2005

This report constitutes the third deliverable of LBNL's contracted role in the FERMI @ Elettra Technical Optimization study. It describes proposed R&D activities for the baseline design of the Technical Optimization Study, initial studies of the RF gun mode-coupling and potential effects on beam dynamics, steady-state studies of FEL-2 performance to 10 nm, preliminary studies of time-dependent FEL-1 performance using electron bunch distribution from the start-to-end studies, and a preliminary investigation of a configuration with FEL's inclined at a small angle from the line of the linac.

1.0 - R&D REQUIREMENTS FOR THE BASELINE DESIGN

The following areas have been identified as requiring R&D, in as much as R&D is required where there are no existing demonstrations of systems or components providing the performance required for the FERMI Project, or experiments are needed in realistic environments to demonstrate achievable performance. The areas identified relate to the baseline design studied for eth Technical Optimization Report, and as such do not include topics relevant to future upgrade possibilities, such as more novel rf photocathode gun configurations – these may be addressed in future studies as needed.

Photocathode laser system spatial and temporal pulse shaping and control
- o UV transverse profile either hard-edge or parabolic, adjustable from 0.1 – 2 mm radius on cathode in seconds or minutes.
- o 1 ps < rise time < 500 fs (flat-top mode).
- o UV longitudinal, either flat-top or parabolic, adjustable in pulse length from 1 – 10 ps FWHM in minutes or hours.
- o 500 μJ UV in shaped pulse delivered to cathode.
- o Variable pulse duration
  - 3-6 ps
  - 9-12 ps
- o Define and test controls interface to laser and diagnostics. Needs to be automated and industrialized.

FEL seed lasers
- o Continuous wavelength tuning from 240 – 360 nm
- o Peak power ~100 MW
  - Cavity enhanced PCPA or other techniques
- o 50 Hz pulse repetition frequency
- o Spatial and temporal pulse profile control (probably not critical).
- o Define and test controls interface to laser and diagnostics. Needs to be automated and industrialized.
- o Wavelength stability.
- o Variable pulse duration
  - ~40 fs to ~100 fs
  - ~1 ps to ~2 ps

Linac, LLRF, and RF power
- o Modulator design
- o Feedback/feedforward systems and integrated LLRF controls
  - Control of beam position and timing
- o Demonstrate amplitude stability of $<1 \times 10^{-3}$ with prototype system
- o Demonstrate 0.1 degree phase stability with prototype

Optical diagnostics
- o Method to cross-correlate seed laser with FEL or spontaneous output
- o FEL seed laser

- Timing relative to the electron beam
  - o FEL output beam
    - Cross-correlate FEL with timing laser
    - XUV autocorrelator and/or FROG
    - Pulse phase and amplitude profile
  - o Undulator multi-diagnostic: determine both size and position of FEL beam and electron beam respectively
  - o Properties of absorption cells and techniques for pulse energy measurement

Electron beam diagnostics
- o Electron beam position monitors with 10 μm resolution
- o Undulator straightness measurement techniques
  - Beam trajectory straight to 10's μm over length of undulator
- o Slice emittance and energy spread at lower energy (< 200 MeV)
- o Non-destructive bunch timing
  - Electron bunch vs. timing system reference
  - Electron bunch vs. seed laser pulse
    - Compton inverse scattering
    - OES (opto electronic sampling)
- o Modulation induced by the FEL seed laser, e.g. XUV coherent transition radiation, electron energy spectrometer
- o RF deflector diagnostic line – measure slice and projected emittance, slice and projected energy spread, and time profile
- o Laser heater as diagnostic for bunch timing, laser energy modulation, slice emittance

Timing and synchronization
- o Long term stability of fiber link stabilized by RF and optical cross-correlation to < 20 fs jitter.
- o Laser-to-RF synchronization better than 20 fs
- o Laser-to-Laser synchronization better than 20 fs

Undulator
- o Develop cost effective strongback with required mechanical attributes
- o Support movers with micron level accuracy
- o Quadrupole fiducialization techniques, in undulator gaps
- o Field quality in a small (~10 mm) gap variable polarization device
- o Automate magnet sorting and shimming

2.0 - PHOTOINJECTOR RF GUN CAVITY DESIGN

PI/ZERO MODE SEPARATION AND PULSED RF DRIVE SPECTRUM

2.1 - Introduction

The high brightness requirement of the electron beam produced by the photoinjector for the FERMI FEL project forces us to examine all possible effects within the rf gun that may result in beam quality deterioration. An issue identified in the current generation of rf guns is the overlap of the lower frequency coupled-cavity mode, the 'zero' mode in a two-cavity structure, that may exhibit a finite overlap in its frequency response with that of the drive pulse from the klystron. As a result, a large amplitude field oscillation may be established that can interfere with the detailed beam dynamics of the emitted electrons with the primary accelerating cavity mode (the 'pi' mode), resulting in beam quality deterioration.

This note is the first of several to study the design of cavities with various frequency separations between the pi and zero modes, to model that excitation of the two cavity modes in a realistic system, and to predict the effects on the emitted electron beam quality. We begin with a study of the cavity modes using frequency-domain and time-domain electromagnetic models. The fundamental strategy and purpose of this study is to increase the resonant frequency separation between the two modes in order to decrease the coupling of the zero mode to the klystron drive pulse. This is one technique for eliminating the effect of the zero mode upon the beam dynamics. Other, more active techniques may also be considered.

2.2 – SUPERFISH Results

The nominal geometry for the rf gun is shown in Figure 2-1 below.

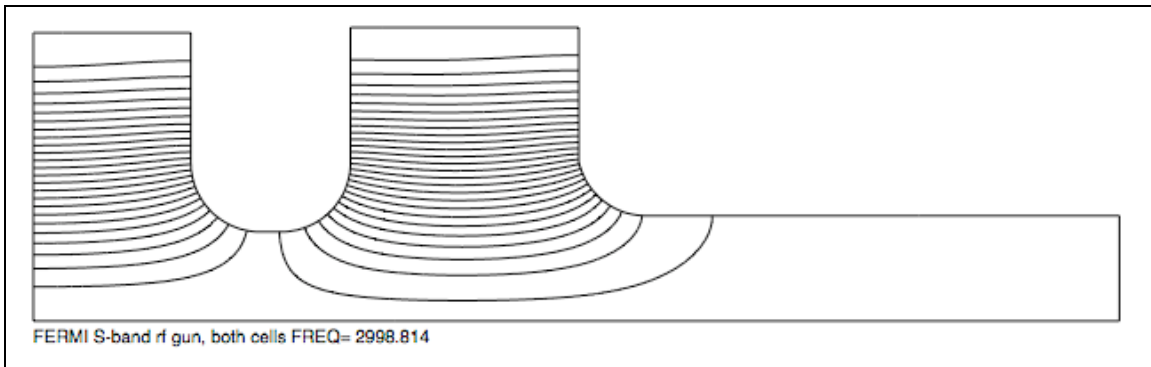

FERMI S-band rf gun, both cells FREQ= 2998.814

Figure 2-1: RF gun geometry from SUPERFISH model. Pi mode field lines are shown.

To produce various cavity tunes and frequency separations between the pi and zero modes, the radial dimensions of the cavity cell walls and connecting iris were adjusted. Increasing the frequency separation between the modes was implemented by increasing the coupling iris radius. The field balance for the pi mode was then re-established by independent adjustment of the two cell outer wall radii. Finally, the pi mode frequency was re-established by tandem (i.e. nearly equal) adjustment of the two cell outer radii. Table 2-1 lists the cavity geometries used to attain the various mode frequency separations.

Table 2-1: Cavity geometry variations and mode tunes (SUPERFISH).

Radius [cm]			Tuning [all in MHz]		
Half	**Full**	**Iris**	**Pi Freq**	**Zero Freq**	**Delta Freq**
3.972	4.045	1.23	2998.830	2995.1	3.71
3.977	4.048	1.25	2998.271	2993.5	4.80
3.998	4.062	1.35	2997.876	2991.5	6.33
4.020	4.070	1.45	2997.751	2998.4	9.33
4.052	4.097	1.58	2997.515	2982.5	15.1
4.089	4.121	1.73	2998.834	2975.1	23.7

The on-axis electric field profiles for the pi and zero monopole modes are shown in Figure 2-2 below. For this study, only a rough field balance (to within ~10%) in the pi mode was required. Nevertheless, most of the geometries studied produced acceptable variations in the pi-mode field balance. The field balance in the zero mode does not exhibit much variation as the frequency separation increases. However, as can be seen in Figure 2-2, the field behavior in the coupling iris region between the two cells does show some trend toward higher fields as the mode separation increases.

As a frequency domain model, SUPERFISH produces accurate values for the geometry dependent shunt impedance ($[R/Q]$) and wall losses (Q_{wall}, from a perturbation calculation). These parameters are listed in Table 2-2 below. The wall losses remain fairly constant for each mode. The shunt impedances are seen to decrease with an increase in the mode frequency separation. This may be offset by re-optimizing the lengths of the to cells, which is being investigated concurrently.
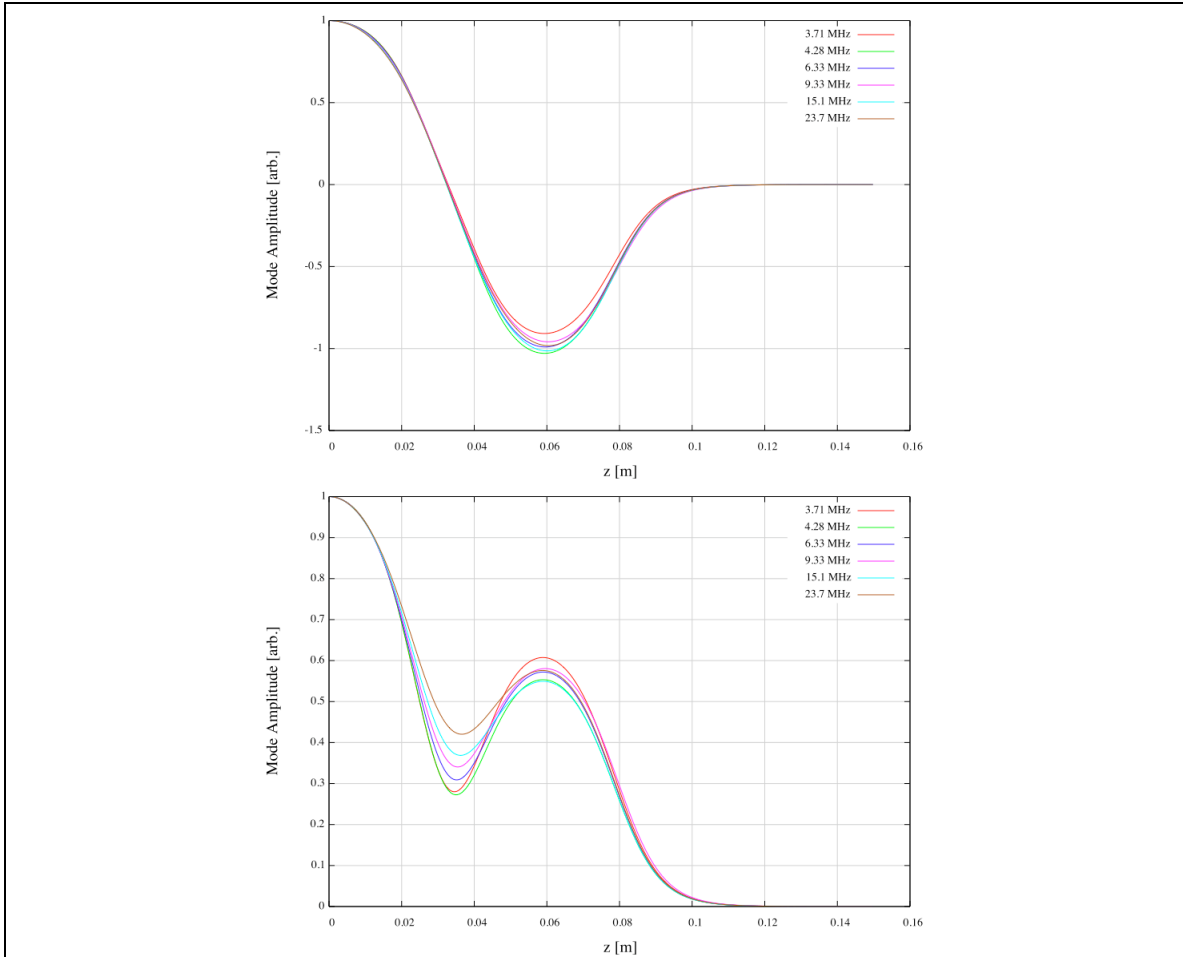
Figure 2-2: Axial electric field profiles for the pi mode (top) and zero mode (bottom), from SUPERFISH model.

Table 2-2: Resonant frequency monopole-mode characteristics

Δ Freq [MHz]	Pi mode		Zero mode	
	Q_{wall}	[R/Q] [Ohm]	Q_{wall}	[R/Q] [Ohm]
3.71	13487	266	12584	5.47
4.80	13690	259	12728	9.52
6.33	13669	255	12813	8.23
9.33	13806	252	12959	7.39
15.1	13816	239	12873	10.7
23.7	13857	232	13043	8.85

2.3 - Microwave Studio Results

A three-dimensional model of the rf gun structure was created and implemented using Microwave Studio from CST (Figure 2-3 below). The cavity is modeled with symmetric waveguides and ports, with full height WR-284 waveguide extending to with 3 mm of the outer cavity walls and a simple, rectangular opening providing the waveguide-cavity coupling iris. The dimensions of the coupling aperture were varied until the time-domain response at the smallest mode frequency separation roughly corresponded to the values measured at the SLAC Gun Test Facility (private communication, John Schmerge). The coupling aperture dimensions were then fixed, as the cell and on-axis iris radii were adjusted to vary the pi and zero mode frequency separation.
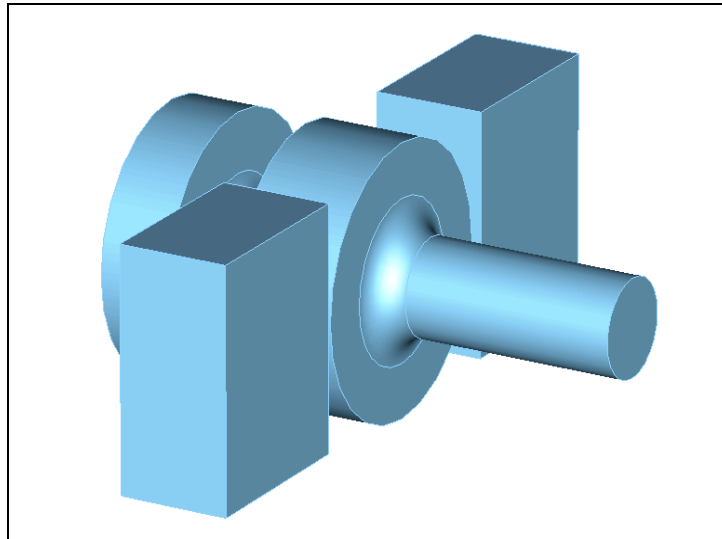
Figure 2-3: Microwave Studio model for the rf gun with dual waveguide feeds.

2.3.1 - Frequency-domain

The frequency-domain results are listed in Table 2-3 below. The axial electric field profiles are shown in Figure 2-4. These results agree well with the SUPERFISH models.

Table 2-3: Microwave Studio frequency-domain results for various pi/zero mode tunings.

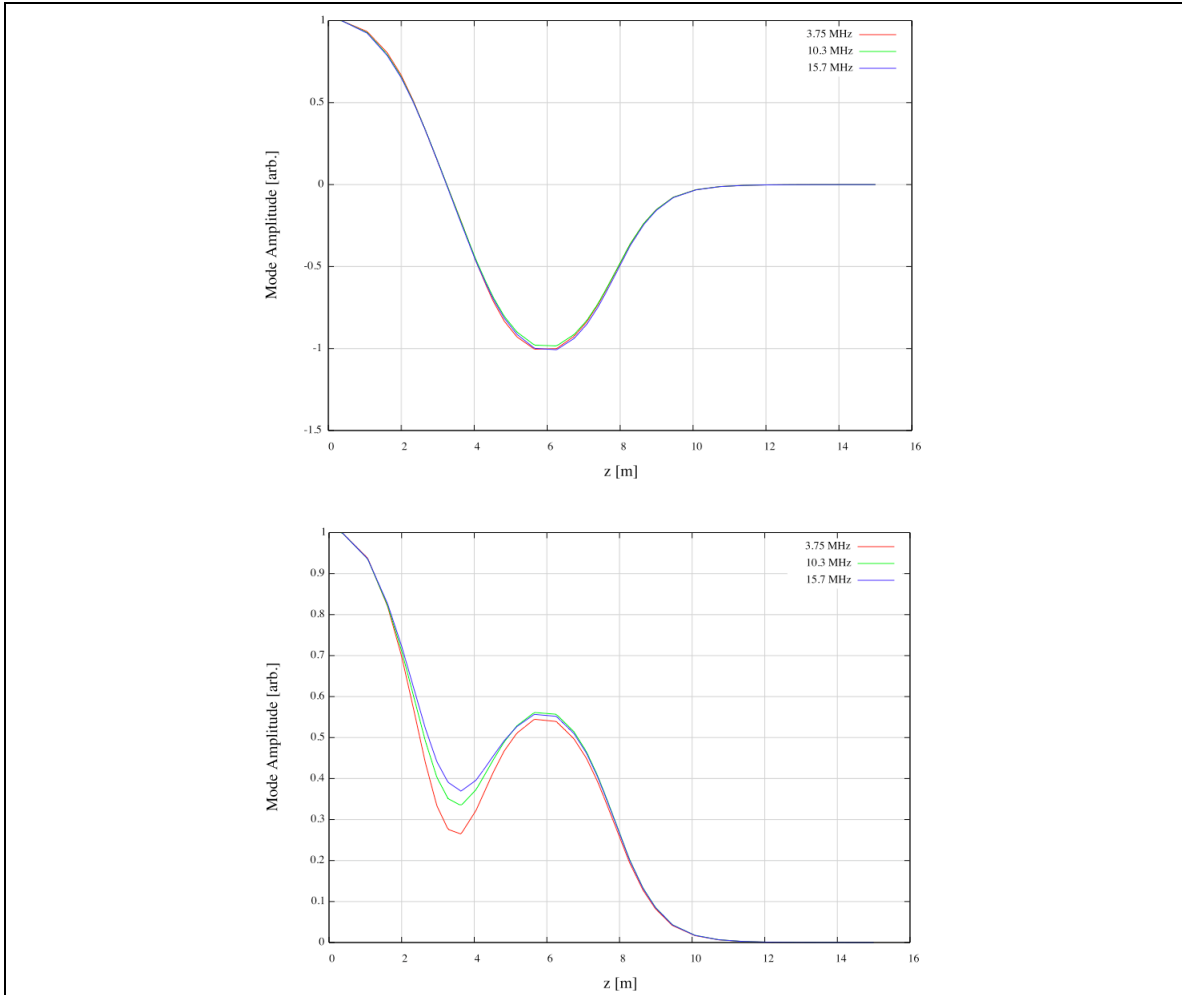| Initial Radius [cm]			Final Tuning [frequencies in MHz]				
Half	Full	Iris	Pi Freq.	Q_{wall}	Zero Freq.	Q_{wall}	Delta Freq.
3.972	4.045	1.23	2998.094	12478	2994.340	12116	3.75
4.020	4.070	1.45	2997.890	12902	2987.600	12419	10.29
4.052	4.097	1.58	2998.540	13041	2982.860	12600	15.68

Figure 2-4: Axial electric field profiles for the pi mode (top) and zero mode (bottom), from frequency-domain Microwave Studio model.

2.3.2 - Time domain

Time-domain calculations were performed in Microwave Studio to calculate the waveguide coupling factors (ß) for the pi and zero modes at their resonant frequencies. The waveguides were tandemly excited in the TE_{10} mode with a flattop signal in the frequency domain with limits between 2980 MHz and 3010 MHz. The reflected signals were then Fourier analyzed, and the complex reflection coefficients calculated. These are shown in Figure 5. The larger radius curve is the pi mode response and the smaller radius curve is the zero mode response. This plot shows us that the pi mode is overcoupled (ß>1) since the response curve encloses the origin, while the zero mode is undercoupled (ß<1) since the origin is excluded. For each of the cases studied, this behavior was seen to be generic.
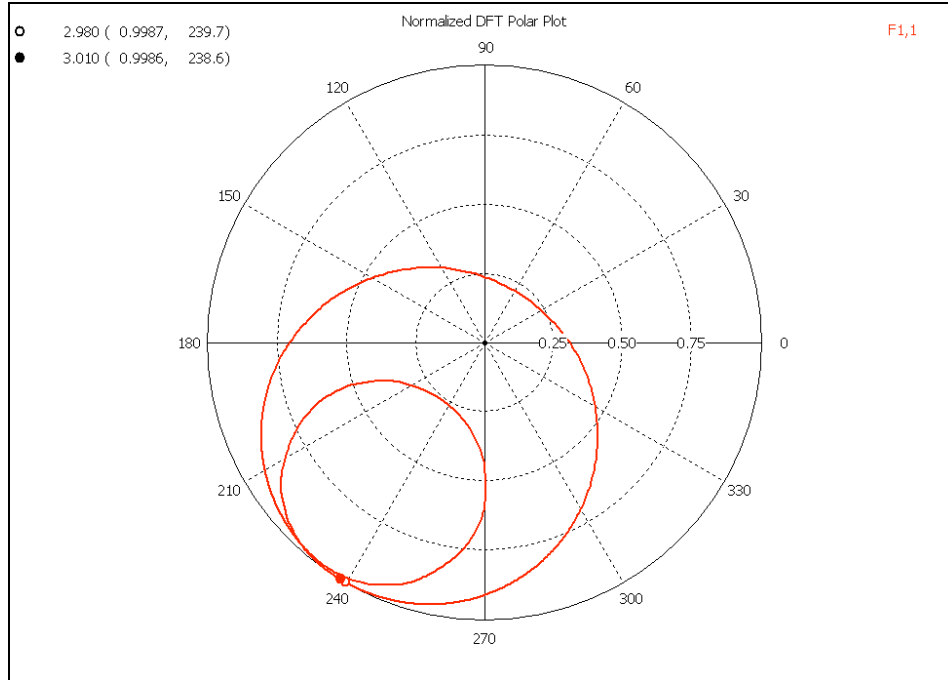
Figure 2-5: Complex reflection coefficient (r) measurement.

The voltage standing wave ratio (VSWR) is calculated from the reflection coefficient (rho) via

$$VSWR = \frac{1 + |rho|}{1 - |rho|} \qquad (1)$$

In the overcoupled case the coupling parameter ß=VSWR, while in the undercoupled case ß=1/VSWR. The results of the time-domain modeling are listed in Table 2-4. Without re-optimization of the input waveguide coupler, the pi mode is well overcoupled, while the zero mode can approach critical coupling. Even after optimization of the coupling to the pi mode, we will expect the zero mode coupling to be a factor of 2-3 smaller.

Table 2-4: Time-domain results for the waveguide coupling parameters.

Δ Freq [MHz]	Pi mode		Zero mode	
	VSWR	ß = VSWR	VSWR	ß = 1/VSWR
3.75	1.558	1.558	1.701	0.588
10.29	1.918	1.918	1.131	0.884
15.68	1.887	1.887	1.220	0.820

2.4 - Klystron Pulse Model and Excitation Spectrum

A model of the klystron pulse that drives the cavity modes has been spectral analyzed. The input pulse envelope is assumed to have a 3μsec flattop with linear, 100ns rise- and fall- times, with single carrier-frequency modulation at 2998 MHz. The spectrum of the amplitude and relative phase of the drive pulse have been calculated and are shown in Figure 2-6, and tabulated in Table 2-5.
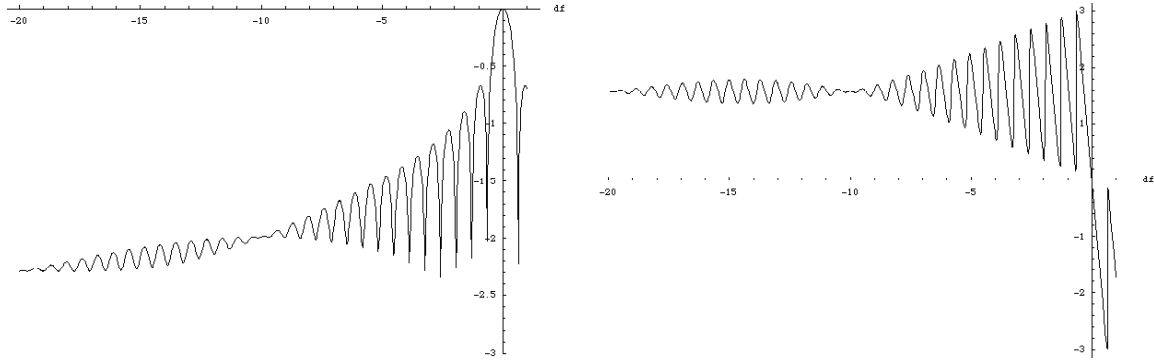

Figure 2-6: Log-amplitude (left) and relative phase (right) of the klystron voltage pulse frequency components, normalized to the 2998 MHz component, versus frequency difference (in MHz).

Table 2-5: Relative amplitude and phase at several frequency separations from the carrier frequency.

Δ freq (MHz)	0	-3.5	-5	-10	-15	-20
Rel. amplitude	1.	0.05164	0.02433	0.01025	0.006981	0.005117
Rel. phase (°)	0.	77.94	122.50	90.	102.01	90.

At large offsets from the carrier frequency and at steady-state, the relative amplitude is seen to decrease exponentially, while the relative phase oscillates about 90°. Hence, a rough expectation is that at steady-state the pi mode will follow the phase and amplitude generated by the component at 2998 MHz, while the zero mode will track with the amplitude and phase shown above. Of course, this estimate does not account for differences in coupling to the klystron pulse for the two modes, nor for mode quality factor differences that determine the actual transient response. That analysis will comprise the next note in this series.

3.0 – FEL-2 EXAMPLES AND STUDIES FOR A MODERATE ELECTRON CURRENT

ABSTRACT: Examples of designs for a short (35 m total length) configuration for the FERMI FEL-2 beamline are presented, and simulation results using GENESIS are shown for a cascade from 240 nm to 40 nm to 10 nm. Based on energy jitter studies, one version is selected as being the most promising. This example exhibits a 48% drop in output power when the electron beam energy is shifted by 0.1%. The baseline case uses a focusing lattice that yields an average beta function of 8 m in the undulator segments which radiate at 10 nm. For the chosen design, various focusing lattices are considered with different average beta functions. The optimum value is 7 m, with a phase advance of 60 degrees per cell. The baseline case seems like a reasonable choice considering the required quadrupole strengths.

3.1 - FEL-2 designs

We consider three different designs for a two-stage harmonic cascade (FEL-2) beamline planned for the FERMI@Elettra FEL. These designs are all examined under the case where a 10 nm output is produced from a 240 nm laser seed at 100 MW peak power, with an intermediate wavelength of 40 nm output produced after the first stage. The electron beam parameters are 1.2 GeV energy, 400 A current, 1.5 micron emittance, and 150 keV energy spread. The total length of the FEL in all three cases is 35 m. The first modulator is 3.04 m long in all cases. The first version has two 2.34 m long undulator segments for the 40 nm radiator, one similar segment as the second modulator, and six 2.4 m long undulator segments for the 10 nm radiator. The second version has three 40 nm radiator segments and five 10 nm radiator segments. The third version is similar to the first but the 40 nm modulator consists of two segments, and five 10 nm radiator segments are used. The configurations are summarized in Table 3-1. Quadrupoles in between the undulator segments focus the beam. In these simulations, the undulators are assumed to contribute focusing in the vertical plane only, except for the final radiator which is taken to have equal focusing in both planes. In any event, most of the focusing comes from the quadrupoles. The optics are designed to result in a matched FODO lattice in the final radiator with an average beta function of 8 m. All simulations were performed using the GENESIS FEL code.

Table 3-1. Parameter sets for FEL-2: number of undulator segments.

# segments	mod 1	rad 1	mod 2	rad 2
Ver 1	1	2	1	6
Ver 2	1	3	1	5
Ver 3	1	2	2	5

In addition to the performance at nominal parameters, we also examine the sensitivity to offsets in the electron beam energy, as shot-to-shot jitter in the electron energy is expected to be a significant source of variation in the output power. The results are given in Table 3-2 and plotted in Figure 3-1 and Figure 3-2, with each case scaled to the maximum power produced. Version 1 produces the most power, with 240 MW for the optimal energy, while Version 2 yields the least power with 210 MW. Version 2 has a slight advantage in terms of the sensitivity to the electron beam energy, with a FWHM of 2.05×10^{-3}. This is true even though the sensitivity calculated for the end of Stage 1 is worse for the Version 2 design, probably because the higher laser power for Stage 2 and stronger bunching going into the final radiator yields more robust performance. The benefit of using Version 2 is modest, but the 13% reduction in peak power is also not severe, and there is a strong preference for an FEL design which produces fairly uniform output from shot to shot. Thus, Version 2 seems like the most promising starting point for these electron beam parameters, and in the remainder of this note all results refer to this configuration for FEL-2.

Table 3-2. Simulations results for FEL-2: output power (in MW) after both stages.

$\Delta E/E$ (10^{-3})	Stage 2			Stage 1		
	Ver 1	Ver 2	Ver 3	Ver 1	Ver 2	Ver 3
-5	0.092	0.0034	0.1	20	24	18
-2	3.1	15	16	91	63	83
-1	148	120	97	116	111	107
-0.5	224	183	173	126	140	116
-0.2	240	205	205	131	157	120
-0.1	240	209	213	132	163	121
0	236	210	217	134	168	122
0.1	225	206	212	133	174	124
0.2	211	201	204	136	179	125
0.5	157	174	160	139	194	127
1	59	101	56	140	213	128
2	3.5	10	0.96	132	217	119
5	130×10^{-6}	110×10^{-6}	1.5×10^{-6}	75	115	65
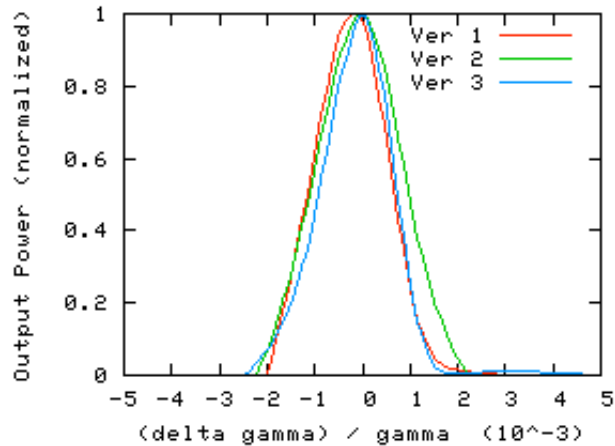
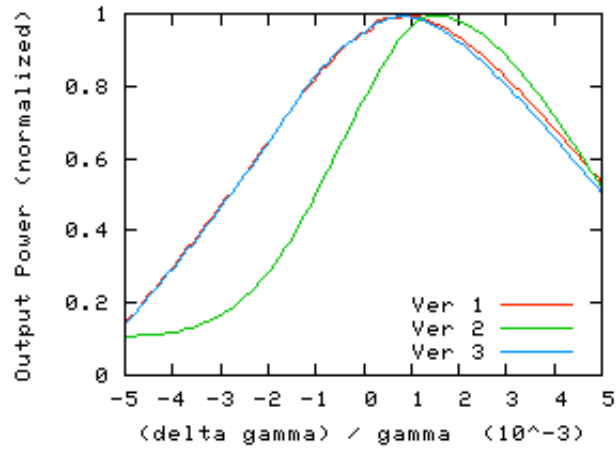Figure 3-1. Output power as a function of electron beam energy deviation, for the three configurations. Results are plotted in terms of power scaled to the maximum power produced in each of the three cases.

3.2 - Performance at 10 nm

Having settled on the Version 2 configuration, the power and bunching as a function of length along the FEL are shown in Figure 3-3. It is also interesting to examine the effect of jitter in the beam energy at different points along the final radiator. The output power and FWHM with respect to variations in beam energy at the end of each undulator segment are given in Table 3-3. Here, the FEL has been extended to allow up to 8 radiator segments in Stage 2. After five undulator segments, a relative shift in beam energy of $\pm10^{-3}$ reduces the power in half. For shorter final undulators, there is less sensitivity to energy. For longer undulators, however, the sensitivity doesn't get any worse because the FEL is already operating in the exponential regime, and the gain length becomes more important than the total length of the FEL. The gain length in terms of power is roughly 5 m.

The choice of beta function is also worth considering. The performance for different choices of average beta function is shown in Table 3-4. Taking 20 cm long quadrupoles, the gradient for an 8 m average beta function is 5 T/m. To reach a beta function of 6 m requires a 7.2 T/m gradient. The results get worse below 6 m, and the lattice becomes difficult. The nominal choice of 8 m looks reasonable, although at 10 m beta function, where the quadrupole gradient is only 3.9 T/m, there is only a 12% reduction in output power.

3.3 - Acknowledgements

Figure 3-2. Power after Stage 1 as a function of electron beam energy deviation, for the three configurations. Results are plotted in terms of power scaled to the maximum power produced in each of the three cases.
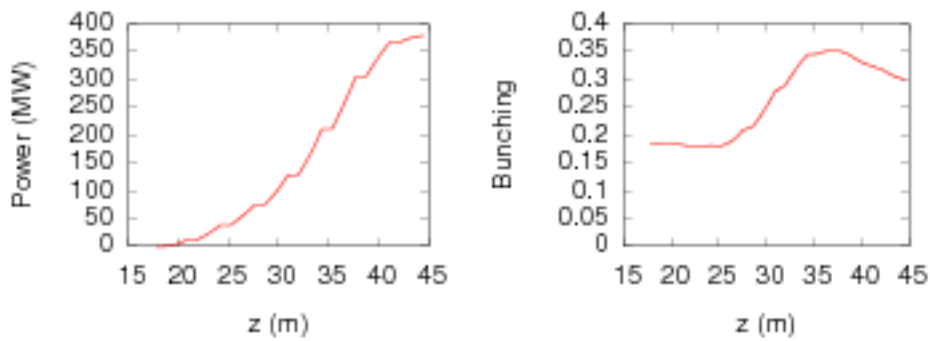

Figure 3-3. Power and bunching in final radiator for Version 2 configuration, as a function of distance.

Table 3-3. Results for FEL-2, Version 2 configuration: power and FWHM in terms of relative energy deviation at the end of each radiator segment.

Segment #	1	2	3	4	5	6	7	8
Nominal Power (MW)	11	37	74	128	210	304	366	378
Relative Energy FWHM (10^{-3})	2.85	2.7	2.35	2.2	2.05	2.05	2.05	2.05

Table 3-4. Results for FEL-2, Version2 configuration: output power for different choices of the average beta function.

Beta (m)	6	7	8	10
Power (MW)	226	226	210	185

4.0 - Extending the Energy Acceptance for FEL-2 at 10 nm

ABSTRACT: We have explored options for decreasing the sensitivity of the FERMI@Elettra FEL output to the average energy of the electron beam. The ability of the FEL to tolerate offsets in beam energy is worse at lower wavelengths, so the given examples all apply to the case of FEL-2 operating at 10 nm. Various methods to achieve this have been attempted. The most successful approaches so far have been adjusting the undulator parameter for each undulator segment and adjusting the phase shifter between segments to apply variable phase shifts between the electron beam and the radiation field. The tolerance levels on fluctuations in beam energy can be increased by up to a factor of two, but only at the cost of a significant reduction (by up to factor of 4) in the maximum beam power achieved.

4.1 - Introduction

One concern related to the performance of the FERMI@Elettra FEL is the sensitivity of the output radiation to the average electron beam energy. If the electron energy varies significantly shot-to-shot, the output power may exhibit large fluctuations which could hinder user experiments. This sensitivity has been seen to become worse as the output wavelength is decreased, presumably because energy offsets lead to temporal offsets relative to the laser radiation field, and the phase error related to a given temporal offset is larger for shorter wavelengths. Without taking any steps to improve the tolerance of the FEL to energy offsets, the relative energy acceptance expressed as the FWHM range of electron energies which yield 50% of the optimum power varies from 8×10^{-3} for 100 nm to 2×10^{-3} for 10 nm output radiation. This has been the motivation for a concerted effort to explore means by which the energy acceptance of FEL-2 can be improved, focusing on 10 nm as an example. The final radiator of FEL-2 consists of six undulator segments, each of which has a 5 cm period and is 2.4 m long, with 1 m breaks between segments.

The example FEL uses a 240 nm laser seed for stage 1, which produces a 40 nm intermediate stage output that is used to seed stage 2. For simplicity, most of the simulations, here using GENESIS, were performed on stage 2 alone using a fixed, 40 nm laser seed as input. This seed roughly matches the nominal output from stage 1. Several promising examples were run for the full FEL-2 case with promising results, although there is the possibility that optimizing on the full lattice could lead to further improvements. At nominal electron energy, and without using any undulator tapering, the output from the laser-seeded stage 2 is similar to the full FEL-2 simulation, yielding about 1 GW at 10 nm. The electron energy acceptance is slightly improved compared to the full FEL-2 case as well, with a FWHM in relative energy offset of 2.5×10^{-3}. A weak tapering brought the total power up to 1.5 GW, also similar to the full FEL-2 simulation, but only a minor improvement in energy acceptance resulted.

4.2 - Strategies to improve energy acceptance

Many attempts at improving the energy acceptance yielded little improvement. These attempts include lowering the energy modulation in the first undulator to 680 keV from 960 keV; reducing the beta function from 10 m to 6 m; increasing the dispersive section above the value which gave optimal power; and applying undulator tapering where each undulator segment was adjusted to have a different undulator parameter, a_W. The only factor that led to a noticeable improvement was having a small increase in the dispersive section, with optimal sensitivity being achieved when the dispersion parameter R_{56} is adjusted to achieve maximum initial bunching at the harmonic, rather than backing off and trying to position the maximum bunching somewhere in the middle of the undulator. The variation in undulator parameter was kept to within 1% in order to match the desired energy acceptance, and although the peak output power did increase the energy acceptance remained roughly the same. Applying a ramp in a_W within each individual undulator segment was also tried, but did not improve the energy acceptance.

The results from Giovanni De Ninno and Enrico Allaria on varying a_W over a wide range, presented in mid-September, looked very promising, as they achieved a much wider energy acceptance although peak power was reduced by more than an order of magnitude. Thus, we considered three additional methods of increasing the energy acceptance: using fewer undulator segments, resulting in lower power but less sensitivity to electron energy; varying a_W over a much wider range, more than 2.5%; and applying a variable phase shift between undulator segments rather than the nominal case where the phase shifter is tuned so that the electrons and laser field remain in phase across each break. The last two techniques are similar, as they both relate to phase slippage relative to the laser field, but complementary. So far, only one or the other technique has been tried; future work will attempt to use both methods simultaneously.

In addition, we have observed that in the nominal design for FEL-2, the second stage modulator was optimized for electron energies slightly below the nominal value. In most of the examples below we have modified the settings so that, given a fixed 40 nm laser input into stage 2, the modulation is maximized at $\gamma = 2349$, the nominal value. In fact, given that the actual input into stage 2 will vary with beam energy as well, and that many of the below examples are skewed towards lower electron energies, it may be preferable to adjust the modulator so that the modulation is maximized at even higher beam energies.

## 4.2.1 - Undulator tapering

In the initial tapering example, a_W varies linearly from 1.1015 to 1.0915. This should correspond to matching relative energy shifts in the range $\pm 1 \times 10^{-3}$, but energy acceptance was only improved by at most 25%. Many variations were attempted in this range. Much larger variations in a_W are considered below. Reducing the length of the final radiator in half, so that only three segments are used, yields 250 MW of peak power and the electron energy FWHM is 3×10^{-3}. While this is not a large improvement, applying large tapering did improve energy acceptance while drastically reducing output power. The least sensitivity to energy was obtained by choosing $a_W = 1.0950$, 1.1120, and 1.1250 respectively for each segment. The first two undulator segments produce power almost

independently, with electron beams at different energy yielding output from one or the other segment, or a little energy from both at the nominal energy. With the addition of the third undulator segment, the situation is slightly more complicated. Although the third segment is tuned to a much higher energy, the overall effect is only to flatten out the variation produced in the same range of energies covered by the two-segment system. Also, the nominal energy yields the peak power rather than a local minimum. However, trying to center the third undulator segment at the nominal energy only accentuates the variation with energy. The final result is an extremely flat dependence on energy over the range of $\pm 3.5 \times 10^{-3}$. However, only 30 MW of power is produced, representing a reduction by a factor of 35 compared to the untapered, 6 segment FEL.

The evolution of power down the FEL is shown in Figure 4-4. The resulting sensitivity to beam energy is shown in Figure 4-5, with a three-section version of the nominal case also shown (with power divided by 10) for comparison. The variation in mode properties for the cases where only two or three undulators are used are shown in Figure 4-6 and Figure 4-7. These results use the original design for the modulator; adjusting this design to the modulator after it had been tuned to be centered at the nominal energy proved to be difficult. Using this three-segment configuration but repeated twice, to form a six-segment radiator, yields much worse performance with large fluctuations in power. This suggests that the evolution of the electron bunch is changing significantly over the length of the FEL.
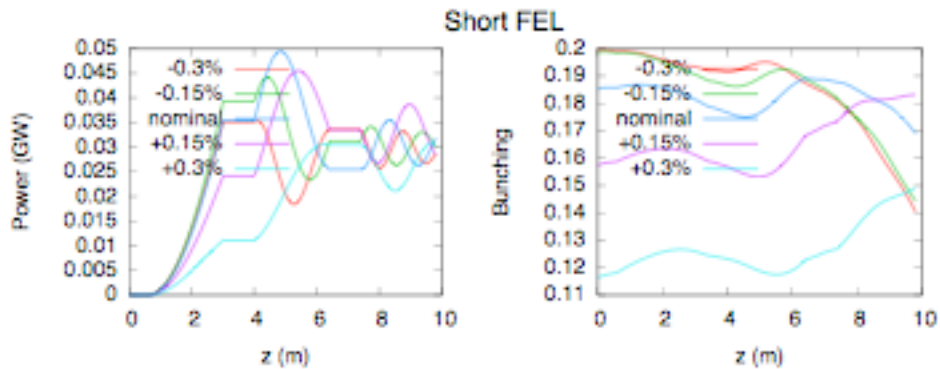
Figure 4-4: Output power and bunching vs. z, for different electron beam energies.
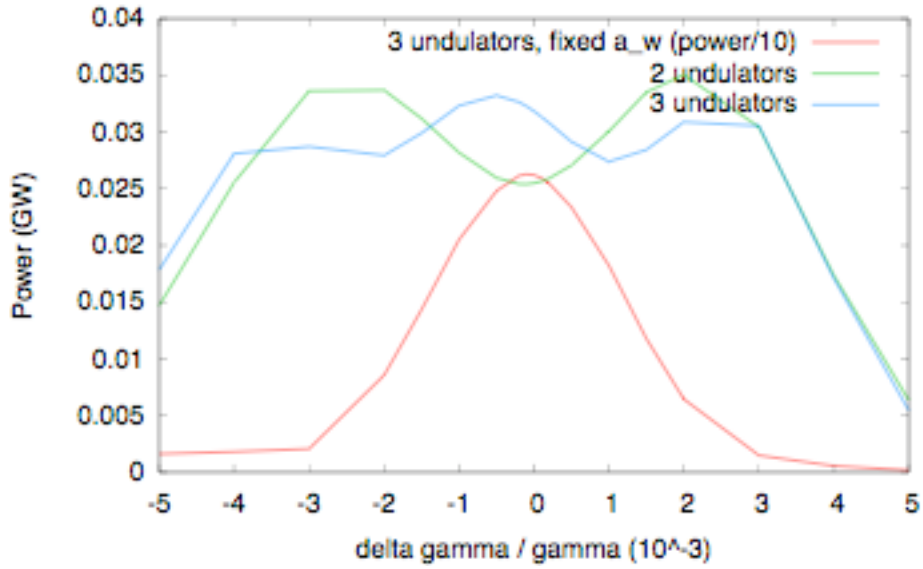
Figure 4-5: Output power as a function of electron beam energy for two or three undulators. For comparison, three undulators at fixed, optimal a_W is also shown (with power scaled down by a factor of 10).
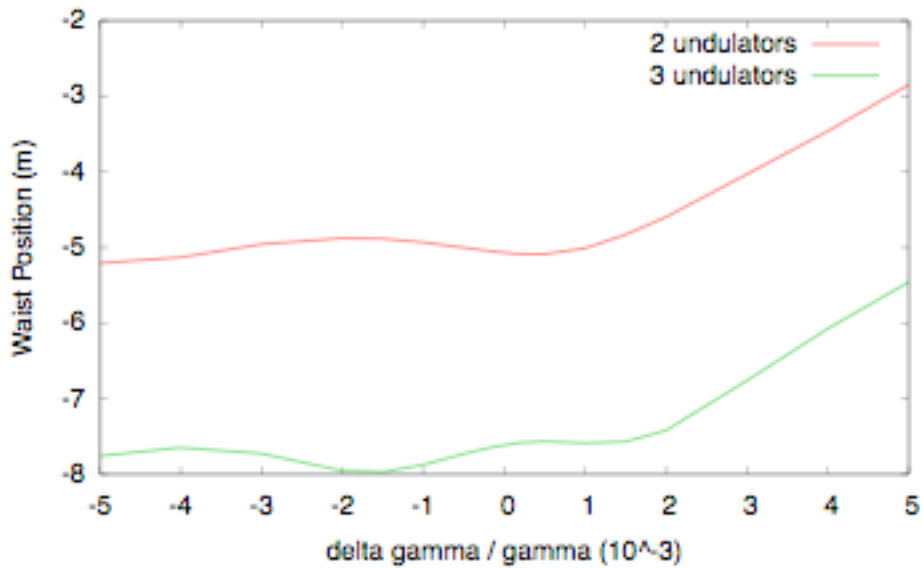
Figure 4-6: Output Location of apparent beam waist as a function of electron beam energy for two or three undulators.
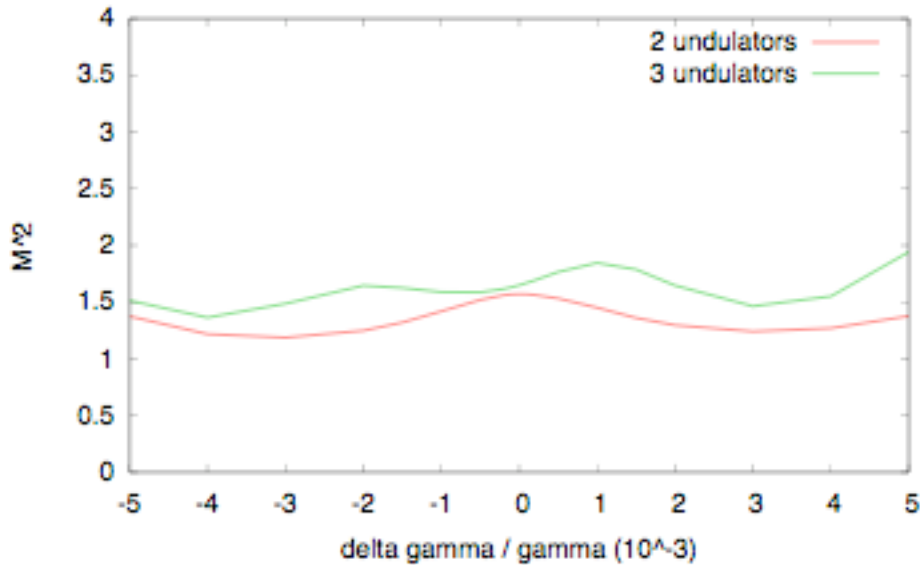
**Figure 4-7:** M^2 parameter as a function of electron beam energy for two or three undulators. segments, two cases with large tapers worked the best.

Using all 6 radiator segments, two cases with large linear tapers worked the best. Here, there was a clear benefit to tuning the modulator section so as to be symmetric around the nominal beam energy, with the modulator a_W changed from the previous value of 2.399 to 2.405. The peak energy modulation of almost exactly 1 MeV then occurs at the nominal energy. The first example, referred to as Taper 1, used the following values for a_W in the radiator segments: 1.1040, 1.0990, 1.0940, 1.0890, 1.0840, and 1.0790. This configuration yields a peak power of 430 MW, and FWHM of 6×10^{-3}. A rough fit to a Gaussian gives an rms of 1.8×10^{-3}, although the variation with beam energy is more uneven. The second example, Taper 2, uses the following values for a_W: 1.1045, 1.0985, 1.0925, 1.0865, 1.0805, and 1.0745. This configuration yields a peak power of 300 MW, with FWHM of 8×10^{-3}. Again, the dependence on energy is not very Gaussian but a rough fit gives an rms of 2×10^{-3}. At reduced beam energies, even an offset of 2×10^{-3} yields a power reduced by less than a factor of 2.

A comparison of these cases with no taper or a weak taper is shown in Figure 4-8 – Figure 4-10. The evolution of power down the FEL at different beam energies is shown for each case in Figure 4-11 – Figure 4-14. Note that Taper 2 works just as well after only five undulator segments.
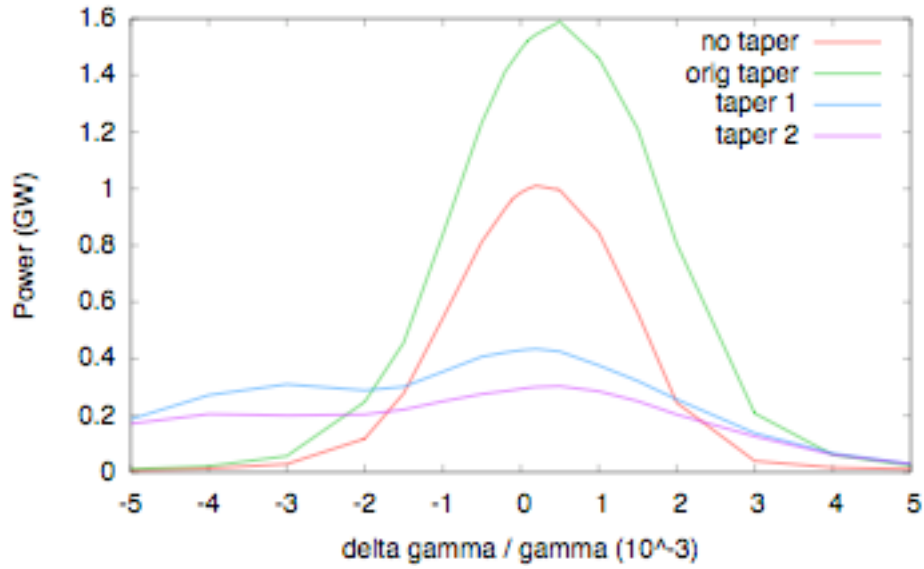
Figure 4-8: Output power as a function of electron beam energy for different tapers.
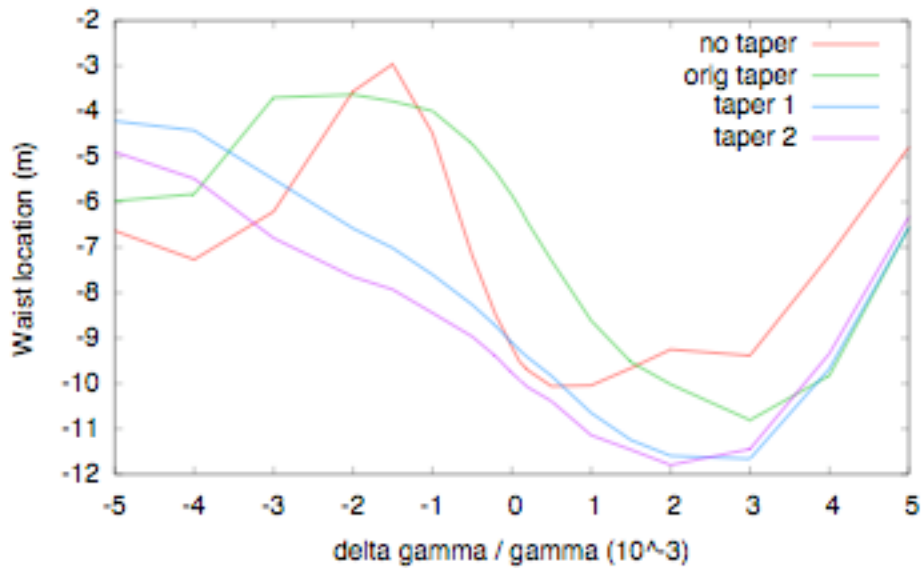
Figure 4-9: Location of apparent beam waist as a function of electron beam energy for different tapers.
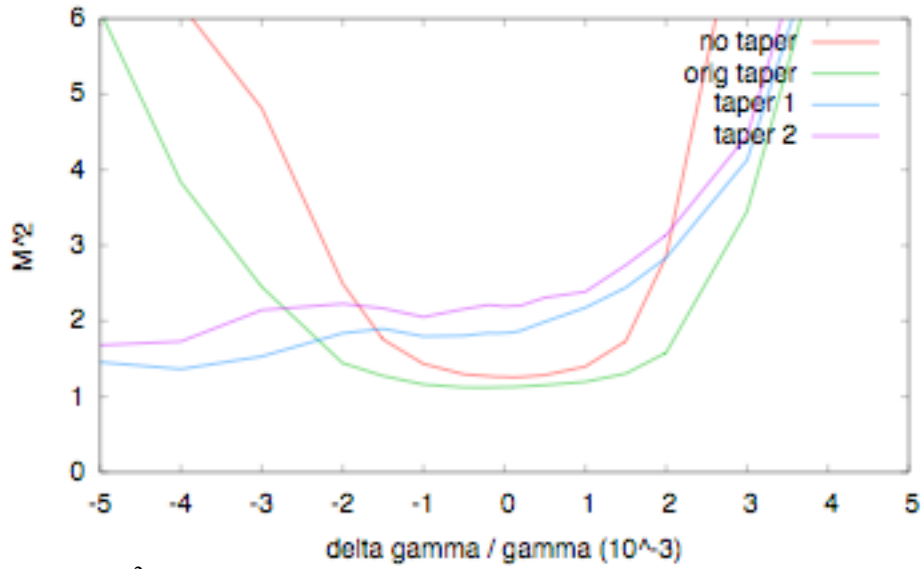
Figure 4-10: M^2 parameter as a function of electron beam energy for different tapers.
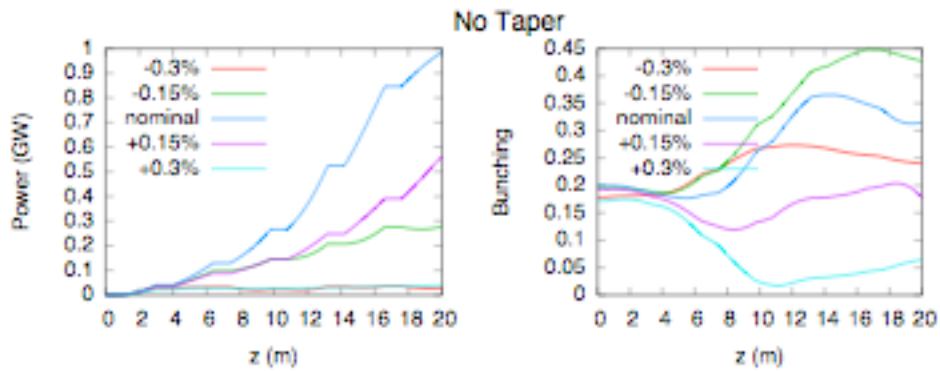
Figure 4-11: Output power and bunching vs. z, for different electron beam energies, no tapering.
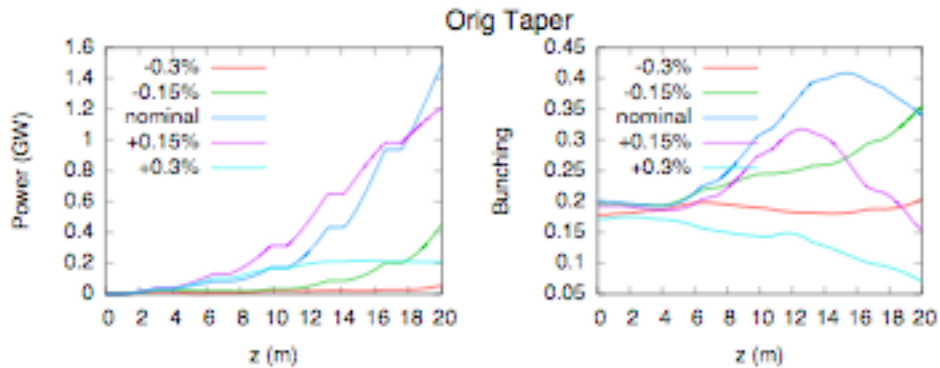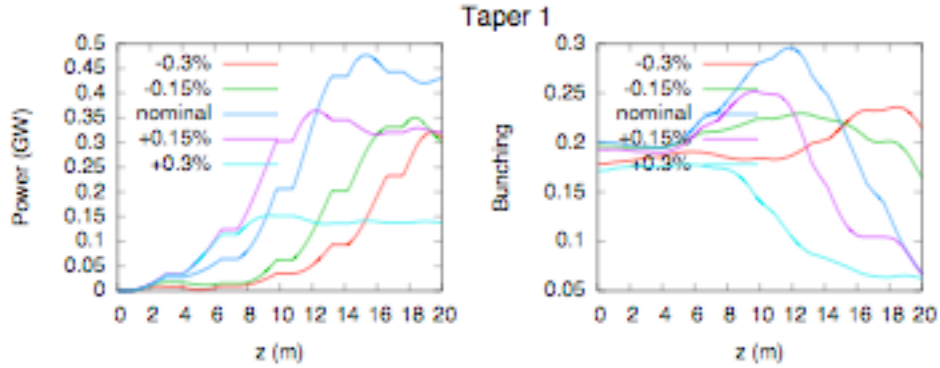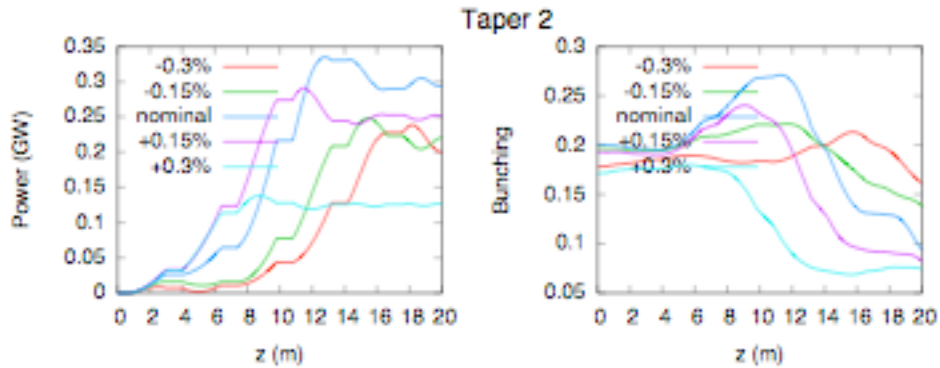

Figure 4-12: Output power and bunching vs. z, for different electron beam energies, original taper.

Taper 1

Figure 4-13: Output power and bunching vs. z, for different electron beam energies, Taper 1.

Taper 2

Figure 4-14: Output power and bunching vs. z, for different electron beam energies, Taper 2.

The power and especially M^2 of the mode almost always seems to become bad at higher energy. Even adjusting the modulator so that the energy modulation was symmetric about the reference energy did not change this. At low energy, the power tapers off much more slowly and the mode quality stays fairly consistent. The bunching is usually much stronger by the last two radiator sections, where lower beam energies interact more strongly. Not surprisingly, the location of the radiation waist moves around significantly in the tapered cases depending on the electron beam energy.

Looking at the evolution of the output power at different energies, some effect of saturation is apparent. At the nominal energy or above, the last two radiator sections contribute nothing. At slightly lower energy, the output power doubles going through the fifth section. At even lower energy, the power keeps increasing through the sixth section, although some of the earlier radiator sections don't work well at all. Overall, it seems very hard to get behavior that is truly symmetric in energy deviation, which complicates the optimization process. In particular, high energies are hard to fit for. This may be related to the fact that the bunching is strongest near the end of the undulator, and interactions in the first few stages modify the beam by the time it reaches the last undulator section.

4.2.2 - Phase shifts

In the previous examples, the break between segments has a phase shifter which is tuned so as to bring the electrons to the same phase relative to the laser field at the end of the break as at the beginning. Below, instead of varying the value of a_W, different phase shifts are applied across the break. Ideally, both techniques should be combined, but this remains to be examined. Three of the most promising cases in terms of energy acceptance for a given peak power, are described below. The first example, termed Phase 1, consists of the following phase shifts across the five breaks: 0°, -30°, -30°, -45°, and –60°. The peak power is 1.2 GW, and the FWHM is 3.5×10^{-3}. The next example, Phase 2, uses the following phase shifts: 0°, -30°, -45°, +90°, -60°. The peak power is 900 MW, and the FWHM is also roughly 3.5×10^{-3}, although the dependence near the peak is fairly flat. The final example, Phase 3, uses the following phase shifts: 0°, -30°, -45°, +60°, -60°. The peak power is 400 MW, and the FWHM is 5×10^{-3}.

These results are summarized in Figure 4-15. For comparison the original linear taper described above is also shown. In Figure 4-16, the evolution of power and bunching along the FEL is shown for the Phase 3 example at different beam energies. The sample energies are shifted to match the shift in optimal beam energy away from the nominal beam energy.
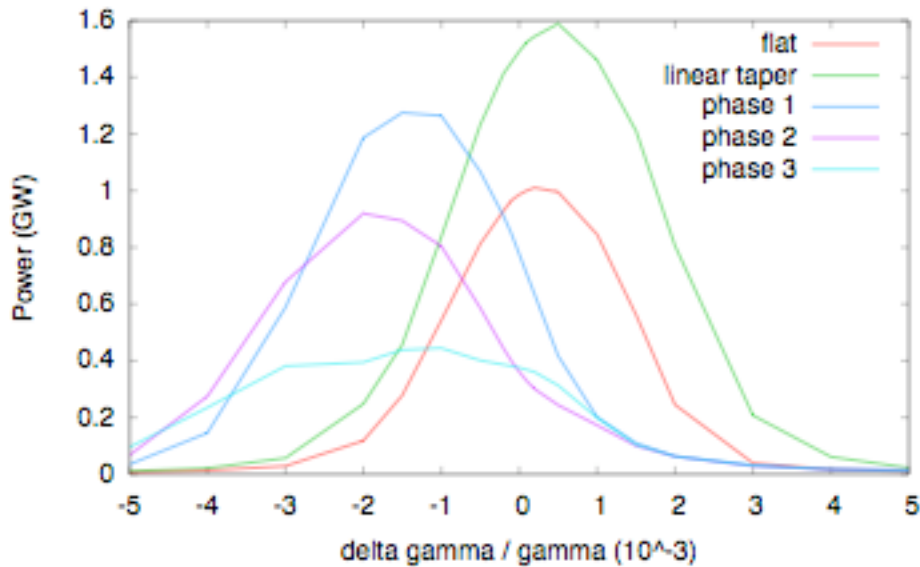
Figure 4-15: Output power as a function of electron beam energy for different phase shifts, compared with a gradual linear taper.
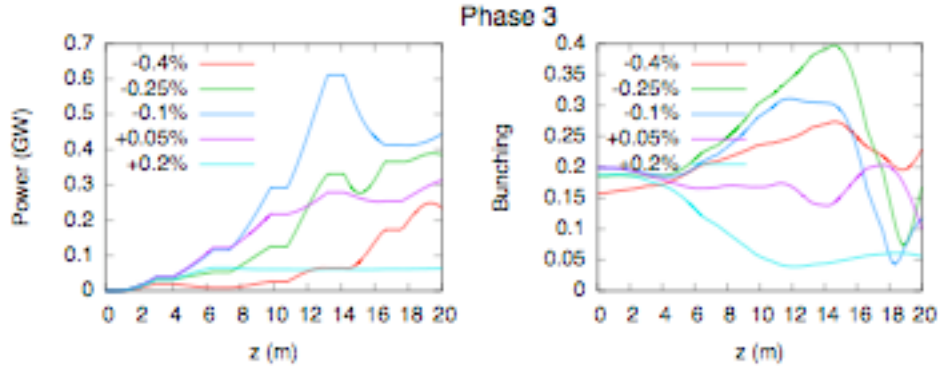
Figure 4-16: Output power and bunching vs. z, for different electron beam energies, Phase 3.

4.3 - Full FEL-2 simulations

One thing to test is to see how these examples work when they receive input from stage 1 rather than from a fixed input seed. Although the results are very sensitive to how the modulator is set up and what values of R_{56} are used, hopefully the slight variation of the output from stage 1 with respect to the electron beam energy does not degrade these results. In Figure 4-17 the results for Taper 2 are shown as implemented in the full FEL-2 configuration using a 240-nm laser seed, with the second stage modulator adjusted to $a_W = 2.405$. The untapered example is also given for comparison. The result is significantly worse than expected at higher energies, but similar at beam energies which are lower than the nominal energy. This is another indicator that the earlier sections of the FEL should be tuned for a beam energy slightly above the nominal value. In Figure 4-18, the results for the Phase 1, 2, and 3 examples are shown for the full FEL-2 configuration, with the modified second-stage modulator. Here the results more closely agree with the simplified model used earlier, probably because the preferred interval of beam energies is shifted to below the nominal value.

Overall, the choice seems to be between a very flat dependence on energy with low power, or a narrower Gaussian dependence with more power. These results, which improve the energy acceptance by up to a factor of two, seem to be comparable to what is seen for FEL-2 at 20 nm using simple tapers, although more work went into achieving these results for 10 nm.
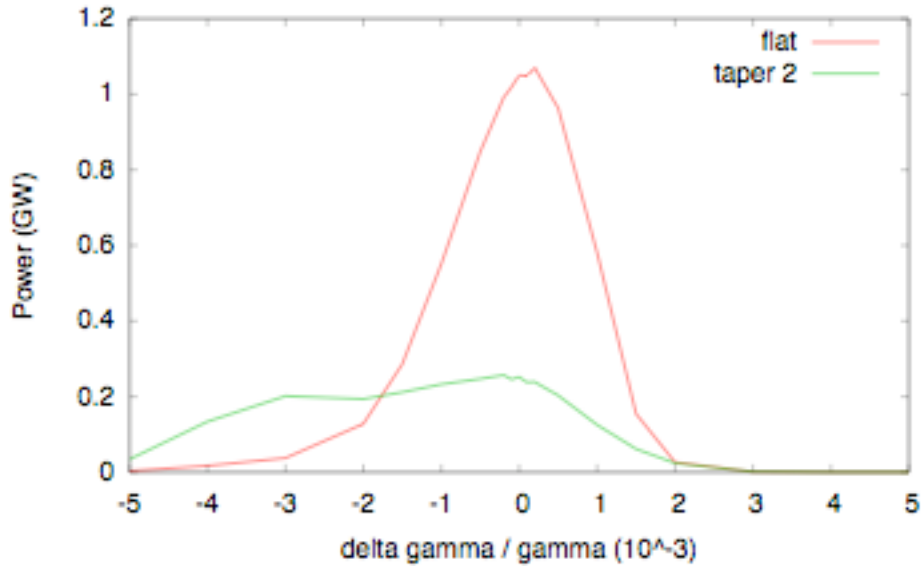
Figure 4-17: Output power from full FEL-2 simulations as a function of electron beam energy for the original, untapered case, and for the Taper 2 example.
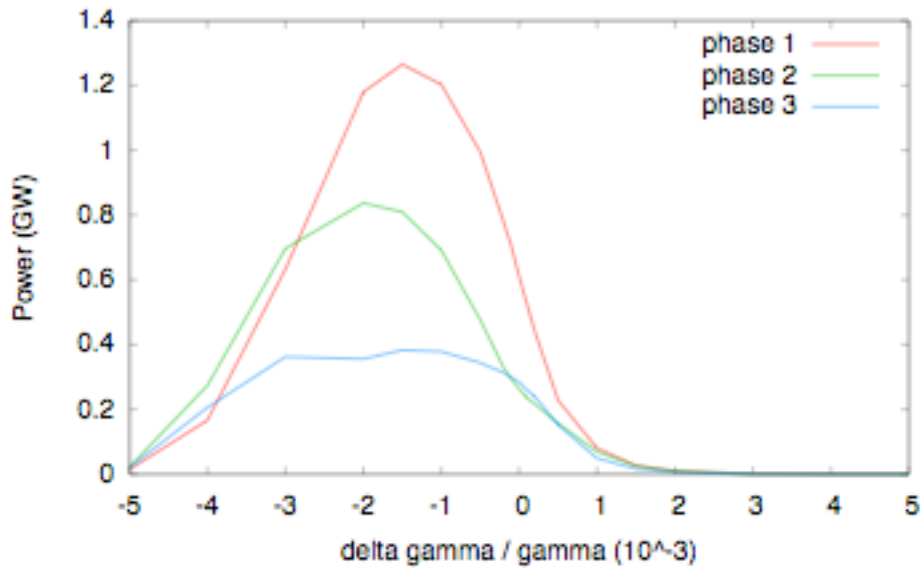

Figure 4-18: Output power from full FEL-2 simulations as a function of electron beam energy for three examples of introducing phase shifts.

5.0 - Time-Dependent Simulation of FEL-1 using S2E produced particle distribution

IN a previous communication, we reported upon time-dependent FEL-1 simulations using the GINGER code importing 6-D macroparticle distributions produced by the accelerator optimization group using the ELEGANT code. That particular distribution included an unphysically high level of space charge instability effects due to numerical limitations of ELEGANT. The results FEL output had relatively poor temporal coherence due to the large temporal oscillations in beam energy.

We have now conducted a new set of GINGER simulations using a new distribution from the accelerator optimization group. This ELEGANT run had the following characteristics: 0.28 nC charge, 8 keV increase in energy spread from a "laser heater", no vertical ramp following the linac, importantly, no longitudinal space charge effects; 10^6 particles; a nominal current ~750 A in the flat portion of the beam (~300 fs duration). The run is named: S_0p28nC_LH8keV_9sep05_NR.sdds. Figures 5-1—5-5 show the characteristics of the electron beam as it enters the FEL.

The GINGER FEL simulation included the following characteristics: modulator: input seed laser at 240 nm, with a constant power of 100 MW, modulator undulator strength a_w=3.924; radiator at 40 nm wavelength: 1.0 fs resolution (300 nm) equivalent to normalized maximum spectral resolution of 3.5×10^{-4} at 40 nm; 384 slices encompassing ~12 slippage lengths; radiator undulator strength a_w=2.400.
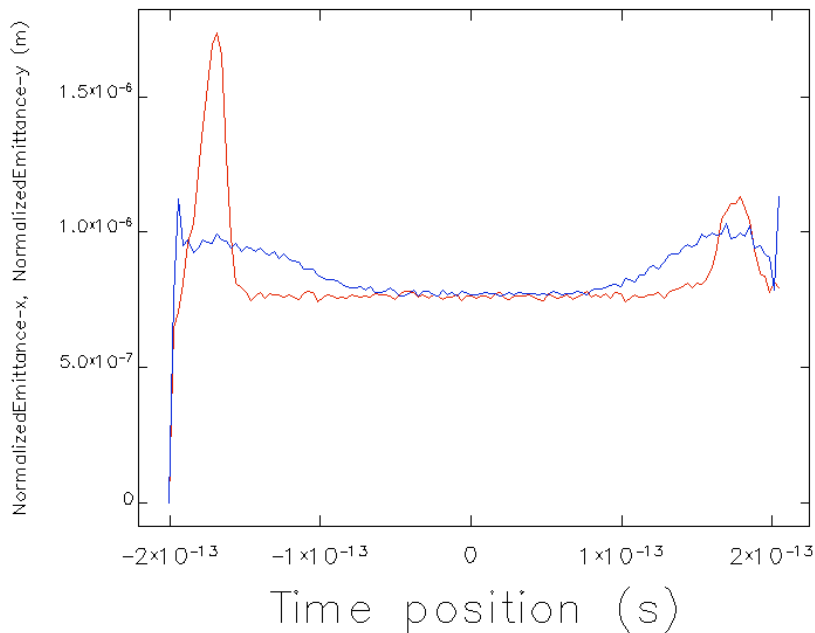

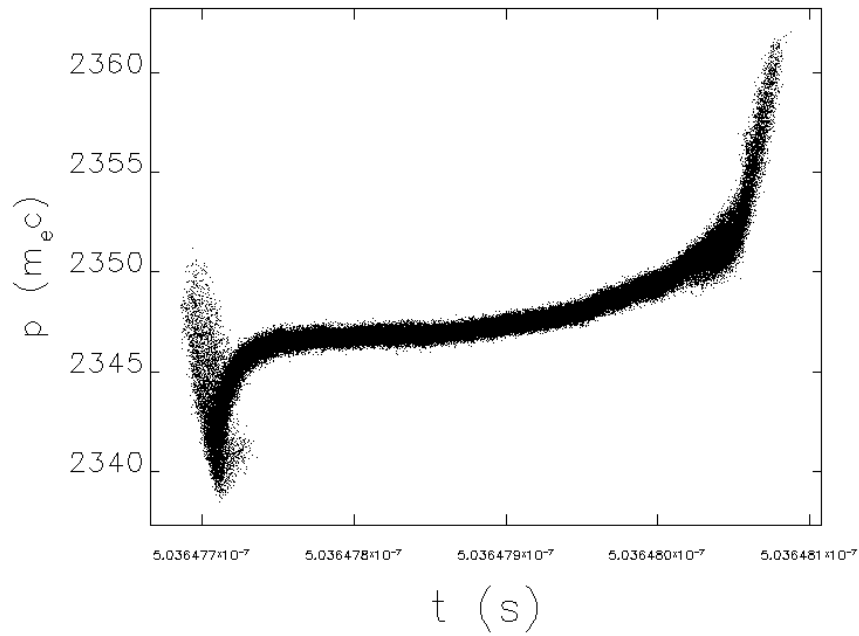Figure 5-1: FEL input beam slice emittance distribution

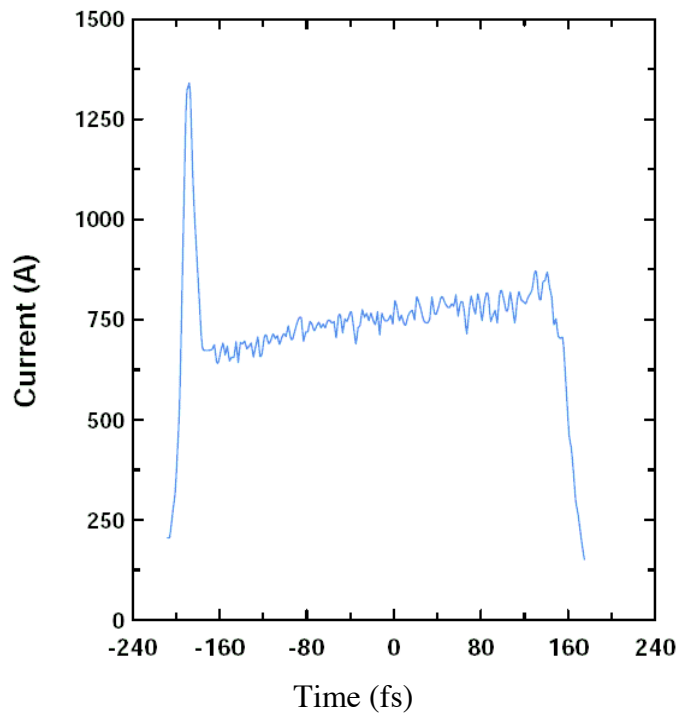Figure 5-2: FEL input beam momentum distribution
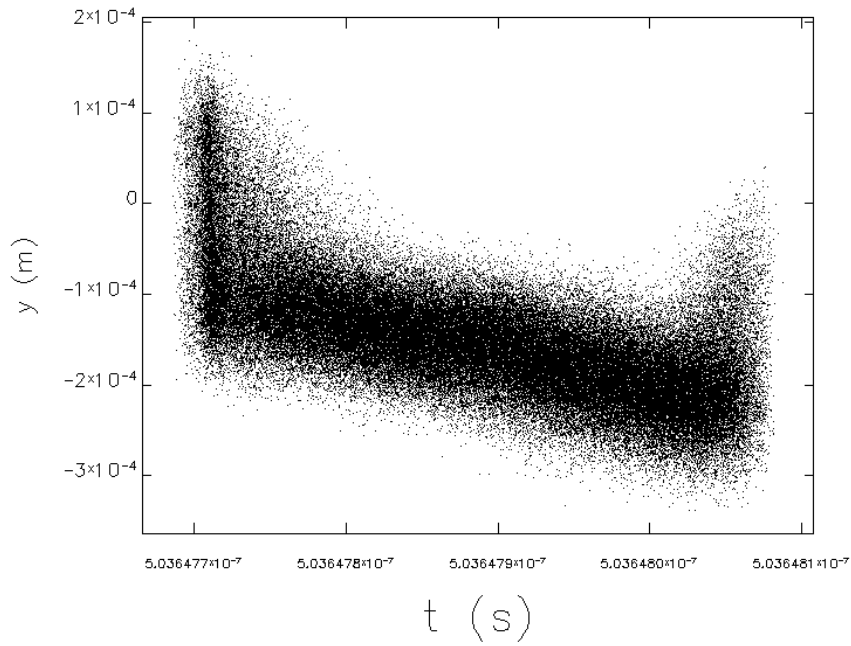

Figure 5-3: FEL input beam current distribution

Figure 5-4: FEL input beam vertical distribution along the bunch
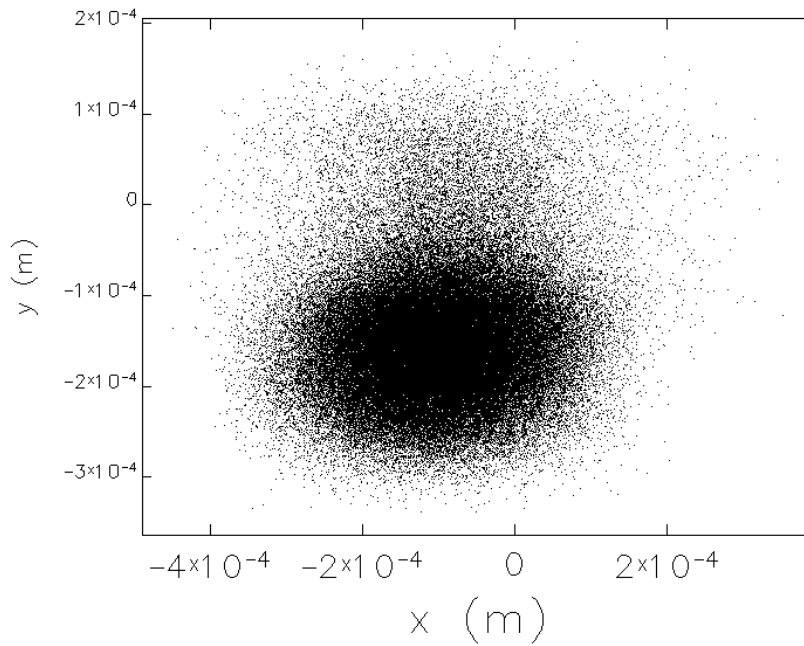

Figure 5-5: FEL input beam transverse projection

The FEL results depicted in Figures 5-6 – 5-7 show that the temporal duration of the output and its spectra quality look quite good. Figure 5-8 shows that the inverse normalized bandwidth reaches a maximum of approximately 800, and the half-power autocorrelation function extends to 50 fs, a 5-times improvement over the previous

results. The output spectrum is reasonably narrow although still more than a factor of two worse than the transform limit. Temporally, the output extends over essentially the entire flat portion of the current pulse with the exception of the tail region where the energy chirp moves the local energy out of the FEL gain bandpass.
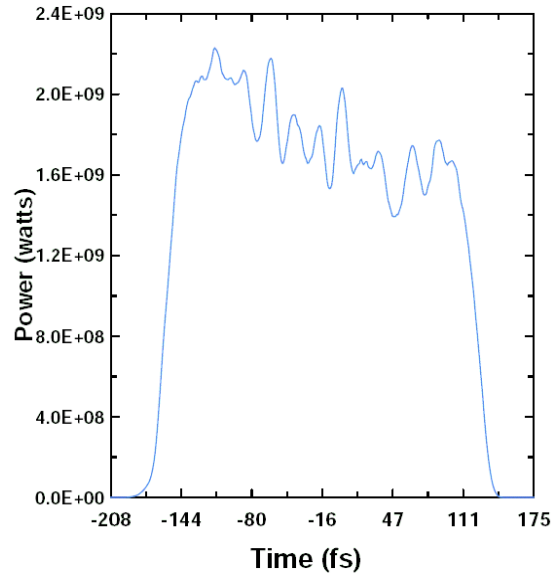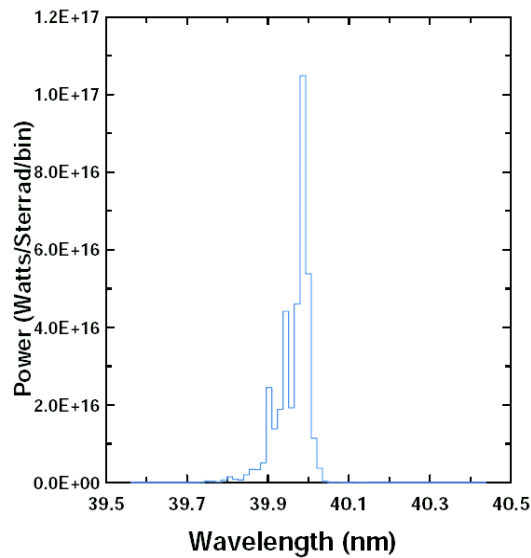

Figure 5-6: FEL output photon beam power profile

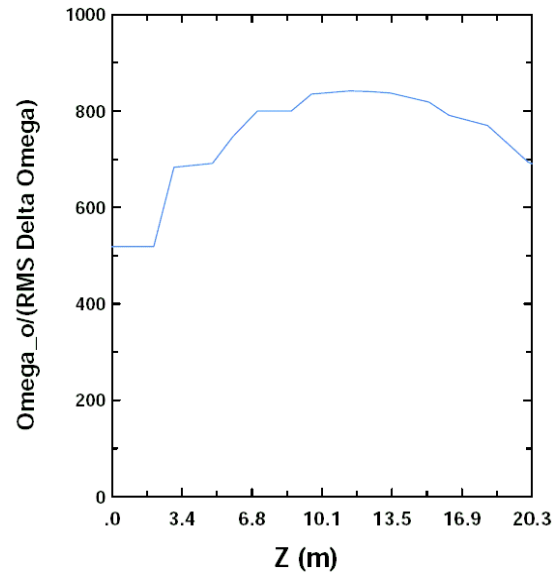Figure 5-7: FEL output photon beam far field spectrum (at z=20.28 m)

Figure 5-8: FEL output photon beam inverse spectral bandwidth as a function of distance along the FEL

6.0 - INITIAL STUDIES OF AN 8° SPREADER LAYOUT

As an alternate option to a configuration with parallel FEL's, we report preliminary investigations into the possibility of orienting an FEL (FEL-1 in this case) at an angle of 8° to the straight-line path from the end of the linac. Orienting FEL's in this manner may have advantages in improved electron beam quality compared to the ore involved requirements for maintaining parallel FEL's, and in layout of the x-ray beamlines and experimental endstations. Figure 6-1 shows the general concept, where an 8° total bend is made of three bends of 2°, 4°, and 2°, with –*I* transform in betatron functions between bends. The –*I* transforms compensate for emittance growth from coherent synchrotron radiation in the bend magnets. Lattice functions for the linac and the 8° spreader are shown in Figure 6-2.
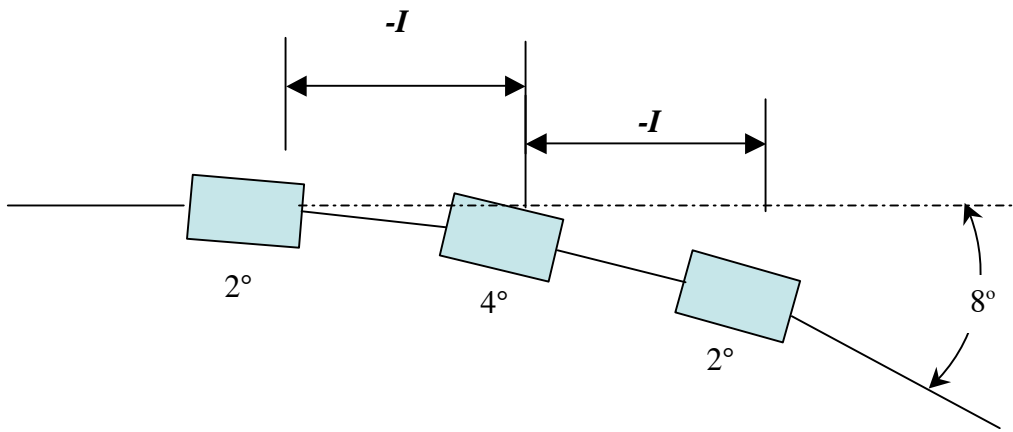

Figure 6-1: Arc providing 8° total bend with two –*I* transform sections to combat emittance growth from coherent synchrotron radiation.

The start-to-end model of electron bunch distributions for this configuration, beginning with the distribution GPT3new1.sdds from the injector, populated with 10^6 particles, and propagated through an ELEGANT model of the accelerator and 8° spreader, is shown in Figure 6-3. Figure 6-4 shows the computed FEL-1 output for this case, with 0.8 μm slice emittance, 0.33 nC, and laser heater at 8 keV, as well as for cases where the emittance has been degraded to 1.2 and 1.5 μm. Good electron bunch characteristics and FEL performance may be obtained with this configuration. Further studies and consideration of other requirements including undulator and experimental hall size and costs will need to be taken into account before adopting such a configuration.
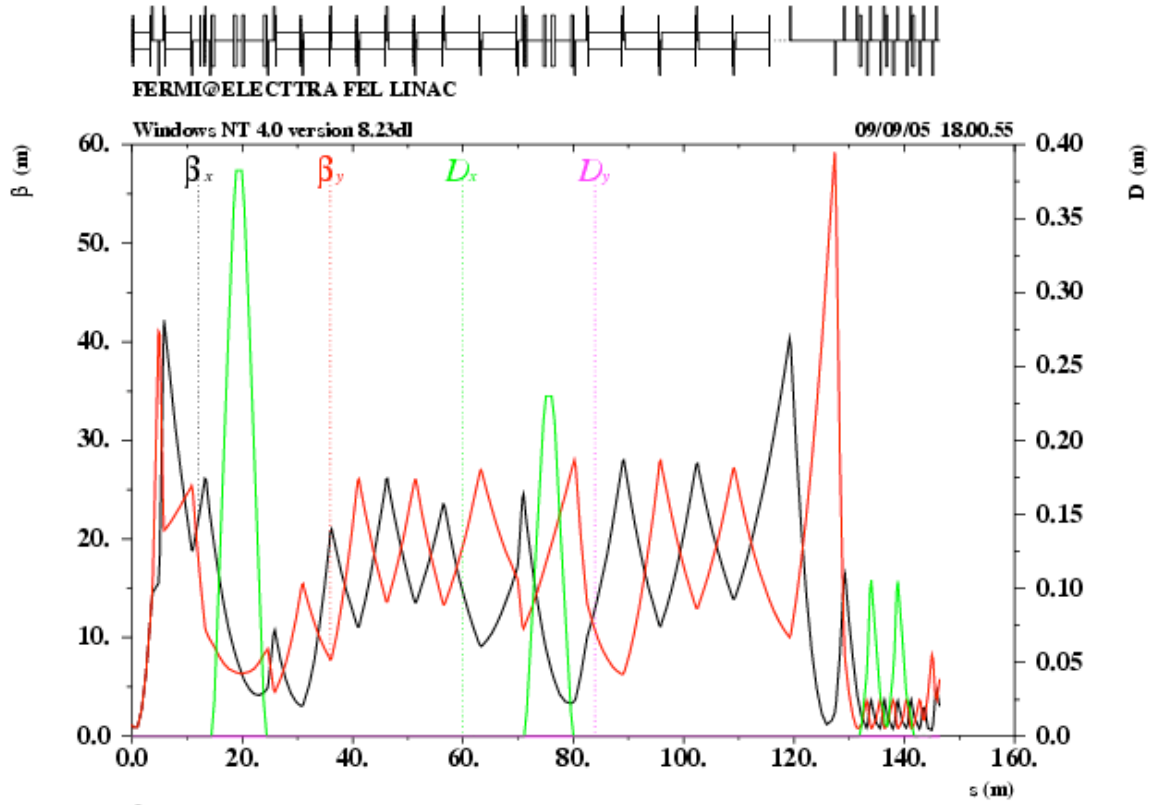
Figure 6-2: Lattice functions for the accelerator and spreader providing 8° total bend
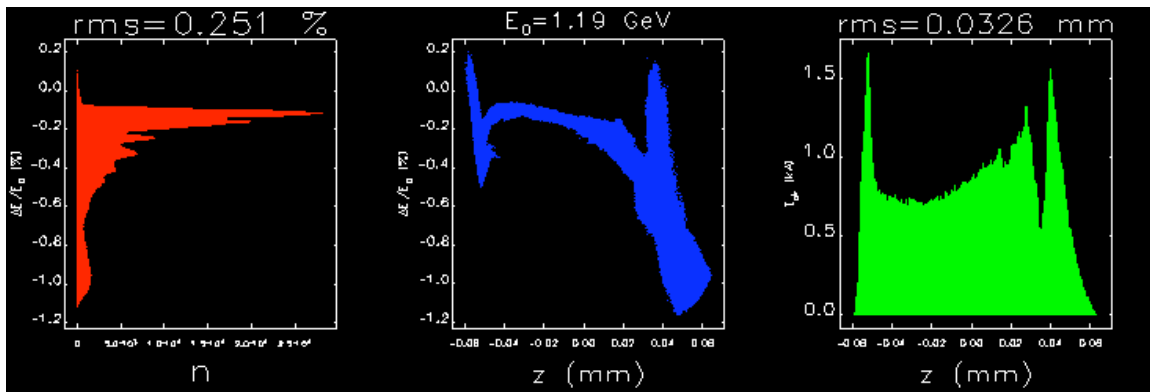

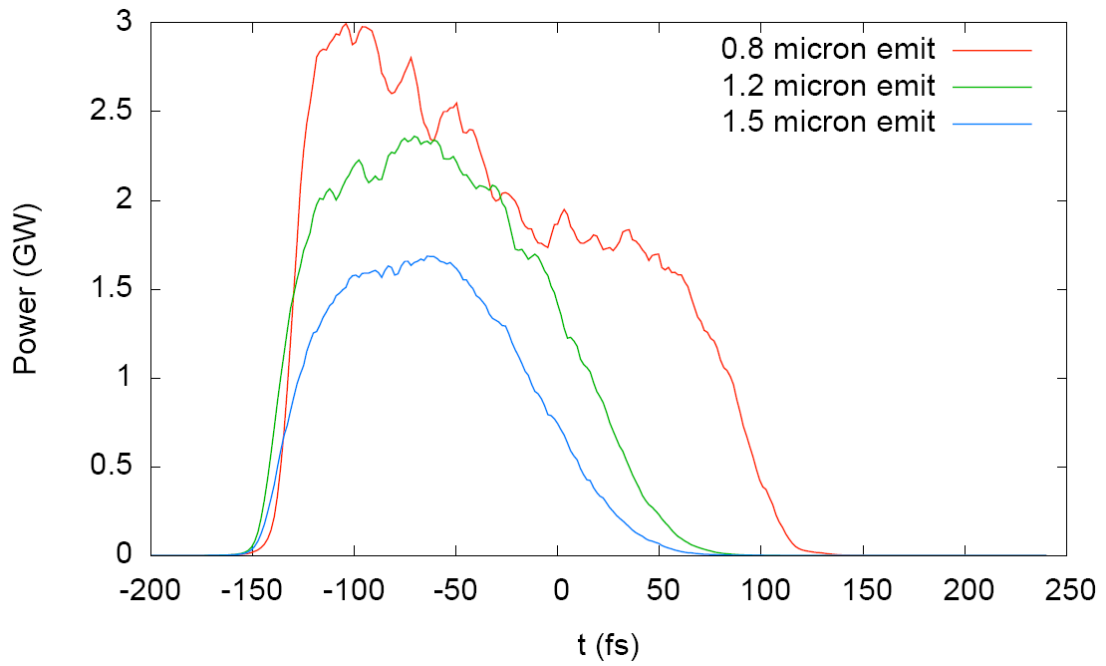Figure 6-3: Electron bunch distributions modeled with ELEGANT

Figure 6-4: FEL-1 time-dependent output for 8° spreader configuration, for three values of slice emittance